A&A 679, A152 (2023)
https://doi.org/10.1051/0004-6361/202346142

Astronomy & Astrophysics

Expansion and ongoing cosmic ray acceleration in HESS J1731−347

V. Doroshenko, G. Pühlhofer, and A. Santangelo

Universität Tübingen, Institut für Astronomie und Astrophysik Tübingen, Sand 1, Tübingen, Germany
e-mail: doroshv@astro.uni-tuebingen.de

Received 14 February 2023 / Accepted 15 September 2023

ABSTRACT

Diffusive shock acceleration in supernova remnants (SNRs) is considered one of the prime mechanisms of galactic cosmic ray (GCR) acceleration. It is still unclear, however, whether SNRs can contribute to the GCR spectrum up to the "knee" (1 PeV) band as acceleration to such energies requires an efficient magnetic field amplification process around the shocks. The presence of such a process is challenging to test observationally. Here, we report on the detection of fast variability in the X-ray synchrotron emission from the forward shock in the SNR HESS J1731−347, which implies the presence of a strong (∼0.2 mG) field exceeding background values, and thus of effective field amplification. We also report a direct measurement of the high forward shock expansion velocity of 4000–5500 km s^{-1}, confirming that the SNR is expanding in a tenuous wind bubble blown by the SNR progenitor, is significantly younger (2.4–9 kyr) than previously assumed by some authors, and only recently started interacting with the dense material outside of the bubble. We finally conclude that there is strong evidence for ongoing hadronic GCR acceleration in this SNR.

Key words. ISM: supernova remnants – cosmic rays – ISM: magnetic fields

1. Introduction

The identification of the acceleration sites of galactic cosmic rays (GCRs) up to ∼10^{15} eV (PeV) energies remains one of the key open problems in modern high-energy astrophysics. Shocks in supernova remnants (SNRs) have been suggested as plausible acceleration sites (Blandford & Ostriker 1978; Drury et al. 1994; Hillas 2005; Ptuskin et al. 2010), and the broadband emission from X-rays to TeV γ-rays observed in several SNRs firmly establishes this object class as accelerators of electrons up to $\gtrsim$TeV energies. However, for individual objects, it is difficult to prove the existence of accelerated nucleonic particles (see Corso et al. 2023 for a recent review). The reason is that TeV γ-rays can have either leptonic (through inverse Compton emission from the interaction of accelerated electrons and ambient photons) or hadronic origins (through π^0-decay from the interaction of accelerated protons and ambient gas). It remains, therefore, an open question which conditions lead to substantial hadronic acceleration in individual SNRs. The detection of 100 TeV–PeV photons from SNRs has long been considered key to identifying hadronic acceleration in those objects. Recent results (Cao et al. 2021, 2023) show, however, that the association of such γ-ray sources with SNRs is not easily made and, even more importantly, that the hadronic-leptonic ambiguity prevails even at these photon energies. This might indicate that proving efficient hadronic acceleration in SNRs up to the PeV range using only the γ-ray channel might be difficult with currently available instrumentation.

Evidence that efficient hadronic acceleration is indeed ongoing can be obtained, for instance, through the detection of the rapid variability in synchrotron X-ray emission from individual shock regions. In Uchiyama et al. (2007) the observed rapid variability of extended synchrotron X-ray emission from the SNR RX J1713.7−3946 was used to put constraints on the magnetic field. Indeed, the expected variability timescale of a population of accelerated electrons that are cooled by synchrotron emission is defined by the longer of the two following characteristic timescales (Uchiyama et al. 2007): $t_{\rm synch} \sim 1.5(B/{\rm mG})^{-1.5}(\varepsilon/{\rm keV})^{-0.5}$ years, the radiative synchrotron cooling timescale of photons with energy, ε; and $t_{\rm acc} \sim \eta(\varepsilon/{\rm keV})0.5(B/{\rm mG})^{-1.5}(\upsilon_{\rm shock}/3000\,{\rm km\,s^{-1}})^{-2}$ years, the acceleration timescale (Uchiyama et al. 2007). The observed X-ray variability in the SNR RX J1713.7−3946 on a year-to-year timescale (Uchiyama et al. 2007) implies, therefore, magnetic field strengths of the order of mG, so acceleration of nucleonic particles is unavoidable as well. The observed variability thus strongly supports a hadronic interpretation of the TeV γ-ray spectrum of RX J1713.7−3946, even if the coherent interpretation of other observables probably requires a more complex scenario than a simple one-zone emission model (Gabici & Aharonian 2014; H. E. S. S. Collaboration 2018). Similar variability has already been reported for Cassiopeia A (Uchiyama & Aharonian 2008), SNR G330.2+1 (Borkowski et al. 2018), and Tycho's SNR (Okuno et al. 2020). While changes in the magnetic field or turbulence properties have also been mooted as a possible driver of the variability in some instances, ultimately it was always concluded that magnetic field amplification is the best interpretation of the data.

Here, we add another example and report similar X-ray variability observations from the SNR HESS J1731−347. We investigate the variability of the X-ray flux in HESS J1731−347 and report two locations in the shock front of the SNR that exhibit variability on a ∼10 year timescale. This provides strong evidence for the presence of strong magnetic fields, and thus field amplification in HESS J1731−347. Together with the fact that electron acceleration is definitively ongoing, our result also

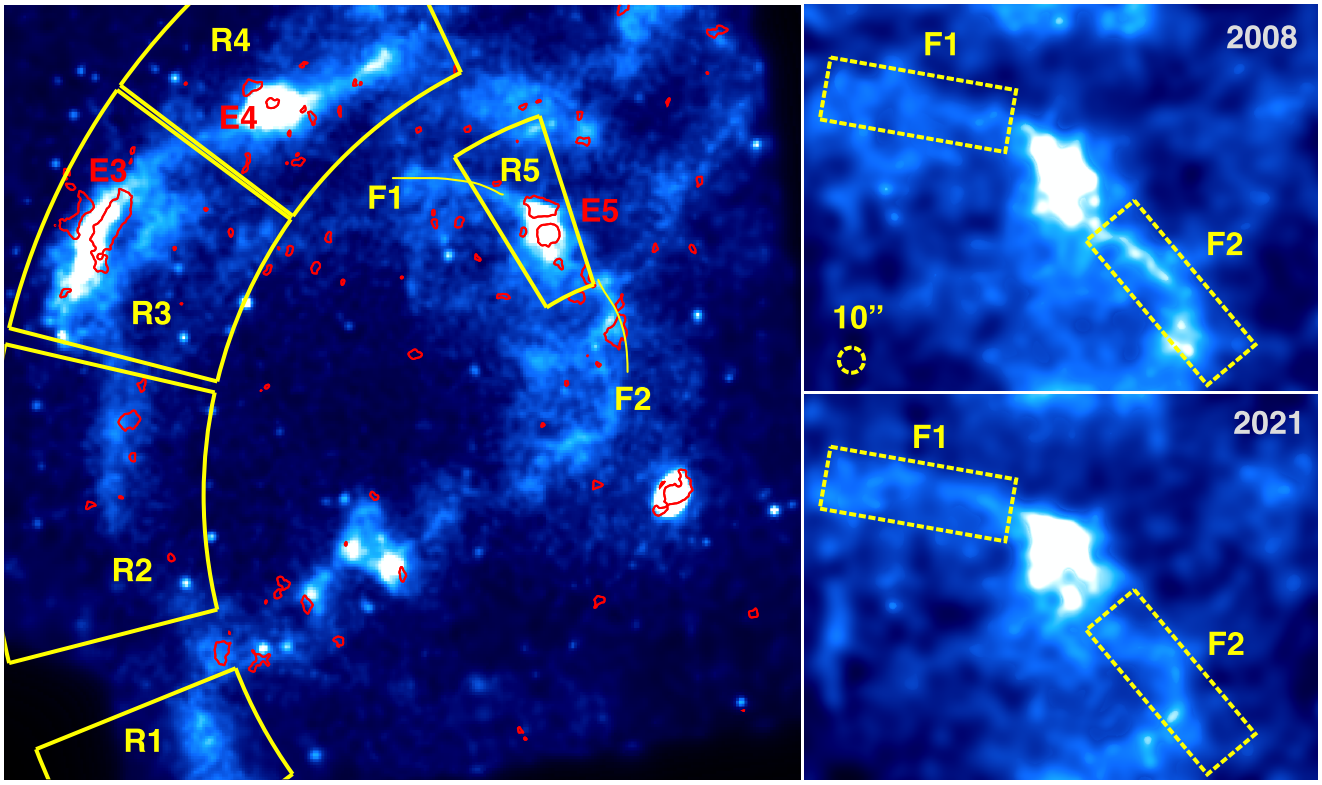

Fig. 1. Overview of the *Chandra* data from HESS J1731−347 in the 0.5–7 keV band throughout the mission's lifetime (left). The red contours show regions that were found to exhibit significant variability (3σ confidence level) between the 2008 and 2021 observations. The yellow sectors (R1–R5) depict regions that were used to obtain the surface brightness radial profiles used to measure the expansion rate of shell parts. The inset on the right shows a close-up view of a bright knot and two narrow filaments (F1–F2) that exhibit a significant flux variability between the 2008 and 2021 observations, as discussed in the text. All images are adaptively smoothed to contain at least 30 counts per pixel to improve visual appearance and are plotted using a linear scale between 0 and 10^{-8} counts cm^{-2} s^{-1}.

implies ongoing hadronic acceleration in HESS J1731−347 irrespective of the interpretation of observed properties in the γ-ray band. We note that earlier attempts to classify at least some of the TeV emission from this object as hadronic were based on the association with molecular clouds at a distance of ∼5.2 kpc (Fukuda et al. 2014), which in the meantime has been challenged by the robust distance measurement of the central compact object (CCO) associated with the SNR of 3 kpc or below (Doroshenko et al. 2022; Landstorfer et al. 2022), although similar arguments can also be made for a gas association at that distance (Doroshenko et al. 2017). Finally, we also measure the expansion rate of the shell at 900–4000 km s^{-1}, which implies an SNR age in the range of 2–9 kyr, in other words significantly lower than an early estimate by Tian et al. (2008) (30 kyr) and consistent with more recent estimates (H. E. S. S. Collaboration 2011; Cui et al. 2016; Doroshenko et al. 2016).

2. Observations and data analysis

To assess potential variability and measure the expansion rate of the SNR shell, we relied on high-spatial-resolution observations of the brightest part of the remnant taken by *Chandra* (Weisskopf et al. 2002). With these goals in mind, we proposed an observation of the region with a configuration that was identical to the earlier observation (ObsID 9139) in order to minimize potential systematic effects associated with the known spatial variations in the point spread function (PSF) and the effective area over the field of view. The second observation (ObsID 22423) was carried out in 2021, 13 years after the first one in 2008. The only difference between the two observation set-ups was the increased exposure of the second observation (by 15%) to compensate for a gradual decrease in the effective area of the telescope due to the accumulation of contaminants on the detector (Plucinsky et al. 2020).

Considering the relatively hard power-law spectrum of the extended emission, extending throughout the energy band covered by *Chandra*, a broad energy band (0.5–7 keV) was used throughout the analysis to ensure high counting statistics. Both observations were reduced using the *Chandra* Interactive Analysis of Observations (CIAO) v. 4.19, following standard procedures described in the instrument's documentation. We also aligned both pointings with a common pixel grid (matching that of the first observation) using the "wcs_match" and "wcs_update" tasks and the coordinates of the 33 point sources detected in both observations with the "wavdetect" tool. The residual offset in the alignment between the two observations is estimated to be ≤0.8″ based on the residual scatter of the point source positions detected in the aligned images. This number is smaller than the estimated errors in the measured shifts of the expanding parts of the shell, and much smaller than the absolute values of the largest measured shifts. Nevertheless, the additional systematic error associated with the alignment of the two observations was accounted for in the further analysis. We note that we also reduced all other available observations of the source with *Chandra*, that is 21340, 22968, 23146, and 23276, to obtain a higher-quality overview image covering a larger fraction of the remnant, as shown in Fig. 1. The additional observations were not used, however, in the quantitative assessment of the

variability due to the significantly lower counting statistics and potential systematic effects related to variation in the PSF over the field of view, as discussed above.

2.1. Variability of extended X-ray emission from the shell

To detect variability from a given sky region, we need to test the hypothesis that the number of counts detected in the two images is inconsistent with being drawn from the same Poisson distribution. Considering that our initial aim is a blind search for variable features in the image (i.e., filaments in the SNR), such a comparison needs to be done for multiple regions, probing the relevant spatial scales (i.e., comparable with the width of the filaments), each containing a sufficient number of counts to make the comparison meaningful. The latter statement is to some extent ambiguous, and is defined by properties (i.e., the algorithms used, the power, and the adopted confidence level) of the statistical test adopted to test the equivalence of the rates from the two regions. To our knowledge, the most powerful test designed specifically for this purpose is the estimated p-values test (E-test) proposed by Krishnamoorthy & Thomson (2004) and implemented in the "statsmodels" package (Seabold & Perktold 2010). This test requires of the order of a few dozen to a few hundred counts (Krishnamoorthy & Thomson 2004) in each of the samples for a robust comparison of the rates, depending on count numbers and the adopted power and confidence level for the test. In practice, we selected the angular scale for the variability analysis based on several considerations. First, the characteristic width of the filaments, in other words the scale relevant for the variability search, is of the order of 15″. This coincidentally corresponds to a region size that contains a few dozen to a few hundred counts for various parts of the image, that is to say it roughly corresponds to the range quoted in Table 1 of Krishnamoorthy & Thomson (2004). Finally, this choice was confirmed empirically, by constructing variability maps as described below for several spatial scales and identifying the smallest scale where random fluctuations still allowed us to visually identify regions of enhanced variability.

The variability maps were constructed by calculating the number of counts and the total effective exposure, both accumulated within a circle with a fixed radius for each pixel in the aligned images of the two observations. The hypothesis was then tested by seeing whether the resulting rates matched each other, using the E-test, as implemented in the "`statsmodels.stats.rates.etest_poisson_2indep`" function. Here, the known differences in the exposure and effective area of the two observations was accounted for by setting the exposure argument of the "`etest_poisson_2indep`" function to the values calculated by the "`mkexpmap`" task in the CIAO package. As already mentioned, we repeated the analysis for several spatial scales and found that the initial best estimate of a region about 15″ in size where variability can be expected and detected is indeed correct. That is, going below this value results in very noisy variability maps (as expected from the properties of the E-test), whereas increasing the region size starts to smooth out variable features, decreasing their significance. Therefore, we fixed the probed spatial scale to 15″ to obtain the final probability map. Here, each pixel encodes the probability that the observed count rates within 15″ match each other in the two observations. The result is shown in Fig. 1, with the contours marking the regions where this hypothesis can be rejected at a confidence level of 3σ and above, in other words marking areas of significant variability.

In the following, we focus on the relevant variable features around X-ray filaments. We note that several small-scale variable regions also visible in the figure (including the region around the CCO) are mostly associated with point sources, and that the apparent variability here is associated with the intrinsic variability of – and residual misalignment between – the images of the two observations, comparable with the pixel and PSF size. That is, masking point sources fully removes this type of variability. On the other hand, several larger regions, including a bright filament in the upper left corner of Fig. 1 labeled R3, a bright knot, and two adjacent filaments halfway through the shell labeled R5, F1, and F2, stand out and deserve a more detailed discussion.

It is noteworthy that the regions around the outer rim of the shell labeled E3 and E4, as well as at the more inner filament E5, where the extended emission appears to be strongly variable, exhibit a two-peaked structure in the probability maps. This is likely due to the radial expansion of the SNR, as discussed below. Several regions where the emission appears to be intrinsically variable can, however, be identified as well. To confirm that this is indeed the case, we first compared the relative brightness of the two filaments adjacent to the knot R5. Whether variability is detected is not obvious from the presented contours at the chosen confidence level. However it becomes apparent when the images are directly compared, as illustrated in the right panels of Fig. 1. That this feature is missed in the blind variability search is largely due to the relatively low brightness of this part of the shell, implying a comparatively low number of counts for the chosen spatial timescale of ∼15″. Considering the observed morphology of the filaments, the use of larger regions containing more counts is, therefore, justified in this case. In particular, boxes with a size of 50″ × 150″, as indicated in Fig. 1, appear to contain most of the flux from both filaments. In total, 966 and 1301 counts in the first observation, and 1052 and 1037 in the second one, respectively, are detected from these regions. The direct application of the E-test to estimate the probability of brightness variability in each of the two regions allows us to reject the hypothesis of equal Poisson rates at a confidence level of $\sim 2\sigma$ and $\sim 5.5\sigma$, respectively, for the two filaments; that is, the F2 region dims significantly, while F1 only exhibits statistical fluctuations, which is also suggested in the visual inspection of Fig. 1.

We note that differences in the effective exposure, the calibration of the contaminant thickness, and the degradation of the detector could in principle affect our comparison above. However, those effects should affect adjacent extraction regions of the image such as F1 and F2 in a similar way. A flux or count ratio is therefore largely insensitive to instrumental changes and should be the same in both observations if there is no intrinsic variability. This hypothesis, that the observed count ratio of the first filament is equal to that of the second, can be statistically tested. To do that, we used the same function as for the construction of the variability maps, namely "`statsmodels.stats.rates.etest_poisson_2indep`", to test the hypothesis that the observed number of counts detected in region F1 in the two observations is consistent with the hypothesis that their ratio is given by their ratio in region F2 (or vice versa). Considering that the observed count numbers are actually random realizations of a Poisson process, we used a bootstrap method to get a more reliable estimate of the significance. In particular, we repeated the test 10^4 times, simulating count numbers in each region and each observation from a Poisson distribution with the rate defined by the observed numbers, and tested whether the ratio is the same for the two regions. As a result we found on average a null hypothesis probability of $\sim 5 \times 10^{-5}$ ($\sim 4\sigma$

confidence level); in other words, the count ratio between observations of the two filaments is indeed statistically different. We conclude, therefore, that the observed relative brightness of filaments F1 and F2 is significantly variable in the two observations at more than a 3σ confidence level, even if the conservative procedure comparing rate ratios outlined above is adopted. The change in relative brightness is likely driven by a change in the brightness of filament F2, as follows from the comparison of the count rates from this region in the two observations. We conclude, therefore, that the observed variability is statistically significant, which is further corroborated by the fact that all identified variable regions appear to be well localized and associated with some of the filaments.

2.2. Expansion rate of the SNR shell

As already mentioned above, the observed two-peaked patterns in the contours reflecting significant variability around the bright filaments E3, E4, and E5 suggest a positional shift, in other words the expansion of the SNR shell rather than intrinsic flux changes. To estimate the expansion rate we constructed partial surface brightness radial profiles around these regions and other parts of the shell containing filament-like structures for both observations. In particular, we integrated the flux within partial annuli with a step size of 2.3″ in the radial direction within the regions R1–5 defined in Fig. 1. Representative profiles from region R3 are shown in Fig. 2. A systematic shift between the profiles obtained in 2008 and 2021 is observed, especially at the outer edge of the filament. Besides this shift, the 2008 profile also appears to be more peaked, that is, the emission morphology appears to have changed, even if it is not trivial in this case to separate the intrinsic variability of the flux from the expansion of the shell. Nevertheless, we attempted to estimate the expansion rate by cross-correlating the radial profiles of the two observations, using a method commonly used to detect phase shifts in radio pulsars as described in Taylor (1992), which is relatively insensitive to minor morphology changes. The uncertainty of the resulting measurements was estimated using the bootstrap method again. For this, the standard deviation of the shifts was estimated by a cross-correlation of 10^4 pairs of synthetic radial profiles (for each region) that were simulated based on the observed number of counts in each radial profile distance bin (assuming a Poissonian distribution and separately for each radial bin). We note that the number of counts in individual radial profile bins is relatively high, i.e. ≥25 in all cases – so bootstrap biases discussed by Picquenot et al. (2021) for Poisson sampling are not expected to play a major role. The results are presented in Fig. 3 and imply an SNR expansion rate of 0.2–0.36 arcsec yr^{-1} (for the shell as a whole and for the well-defined filament, R3, shown in Fig. 1).

We emphasize that in the presence of intrinsic variability it is not possible to fully decouple it from the shell expansion as a whole, so some caution is needed when interpreting the estimate above. This is illustrated by the large offset measured for region R5, as shown in Fig. 3, which appears to be much larger than expected given its position. This is likely caused by the intrinsic variability visibly affecting the morphology of the extended emission here (see e.g., the right panels of Fig. 1). We interpret the fact that this region appears to be an outlier as a further indication that emission not only from filaments F1/F2 but also from the knot R5 itself appears to be variable. For this reason we consider any offset value measured for this region to be unreliable and exclude it from further calculations.

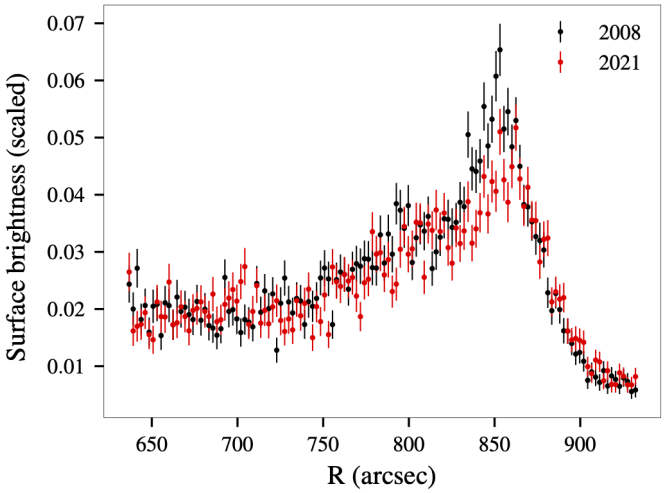

Fig. 2. Radial profiles of the X-ray surface brightness at region R3 (defined in Fig. 1) measured in 2008 and 2021 *Chandra* observations, in the 0.5–7 keV energy band.

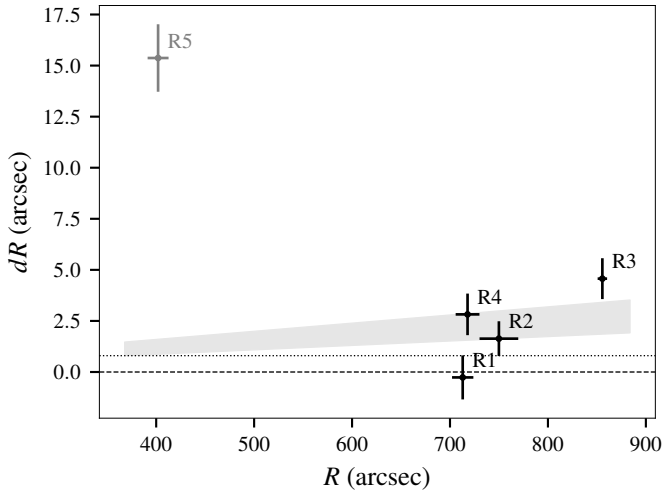

Fig. 3. Offsets measured for various parts of the shell (R1–R5) defined in Fig. 1, as described in the text. The grey band shows the 1σ expectation for the offset as a function of distance, assuming a uniform expansion as obtained by a joint fitting of the regions R1–R4 (that is, excluding the outlier region, R5). The horizontal lines correspond to zero offset and a 0.8″ estimated uncertainty, from the alignment of the two observations.

Amongst the examined regions, the largest shift is measured for region R3, where the outer rim is also best defined. Nevertheless, we attempted to estimate the overall expansion rate by fitting all four remaining regions (R1–R4) simultaneously. We assumed a linear expansion, that is, $dR \propto R$ expected for a spherically expanding shell, and directly fitted the simulated data used to obtain the points in Fig. 3. In practice, the Bayesian inference package "`ultranest`" Buchner (2021) was used to derive the parameter values and uncertainties. The likelihood function was defined assuming a normal distribution with a 0.8″ width to account for any residual uncertainty from the alignment of the two observations (indicated in Fig. 3 with a horizontal line). As a result, we estimate a maximal shift of 2.6(1.1)″ for the outer radius of 855(5)″, which translates to an expansion rate of ∼0.1−0.3″ yr^{-1} and makes HESS J1731−347 only the second of the spatially resolved TeV SNR shells

(besides RX J1713.7−3946, see e.g., Tsuji & Uchiyama 2016; Acero et al. 2017; Tanaka et al. 2020) for which such a measurement is available. The kinematic age of the shell can then be estimated at 2.4–9 kyr, and the shock velocity at 900–4000 km s^{-1}, under the assumption of a constant forward shock velocity and a distance of 2.5 kpc (Landstorfer et al. 2022). These results appear to be consistent with more recent literature estimates (H. E. S. S. Collaboration 2011; Cui et al. 2016; Doroshenko et al. 2016).

3. Discussion and conclusions

Our study is based on a comparison of two X-ray observations of the brightest part of the SNR shell of HESS J1731−347, taken with the *Chandra* observatory in 2008 and 2021, 13 years apart from each other. The second observation was specifically geared towards the search for variability and to measure the expansion rate of the shell, and was therefore set up to fully replicate the former one. This enables a straightforward and robust comparison of both observations to be performed, without introducing systematic effects associated with variations in the PSF and the effective area over the field of view of the instrument. In particular, it enables us to conduct a blind search for variability sites by means of a direct comparison of the count rates in individual observations. We conducted such a search and constructed a variability map, shown with red contours in Fig. 1. Several regions with highly significant brightness variations ($\geq 3\sigma$ for spatial scales of $\sim$15″) between the two observations are identified. The variability of these regions could either be due to the expansion of the shell or it could be intrinsic. The variability observed in several regions along the outer rim of the shell appears to be mostly associated with the expansion of the shell, whereas the variability of several filaments within the inner part of the remnant is almost certainly intrinsic. Indeed, the highly significant variability of the relative brightness of the two filaments adjacent to the knot R5–E5 can in no case be explained by the expansion of the shell, and thus shows that the intrinsic flux is definitively variable.

We conclude, therefore, that the observed X-ray emission from HESS J1731−347 is indeed variable on a timescale of a few years. Similar variability observed in RX J1713.7−3946 has been attributed (Uchiyama et al. 2007) to ongoing particle acceleration and used to derive a lower limit for the magnetic field strength at the shock. The same arguments can be applied to HESS J1731−347, implying a lower limit of the magnetic field strength of $\sim$0.15–0.19 mG, which also strongly supports the hypothesis of efficient ongoing nucleonic acceleration in this case. We note that variability can in principle also be related changes in magnetic field strength or magnetic turbulence, so the detection of variability itself cannot be considered smoking-gun evidence for ongoing nucleonic acceleration. On the other hand, for HESS J1731−347 the highly significant difference of the azimuthal dependence of the X-ray or radio and TeV surface brightness (Doroshenko et al. 2017) has already been used to argue for at least a partly hadronic origin of the TeV emission in the dim, western X-ray part of the shell. More importantly, the observed variability is confined to the opposite part of the shell, which indicates that the acceleration is currently ongoing throughout large parts of the shell.

We observe that HESS J1731−347 appears to have similar characteristics to RX J1713.7−3946, besides the X-ray variability detection. Both are remnants of core-collapse supernovae that exploded in a wind bubble blown by the progenitor, and only recently did their ejecta begin to interact with a dense interstellar medium (ISM) at the edge of the bubble (Cui et al. 2019; Doroshenko et al. 2017; Fukui et al. 2021). For both sources, expansion in a rarefied ISM can explain the still-high shock velocities, despite their large physical sizes of several tens of parsecs and ages of several thousand years. High expansion speeds and high ISM densities are, in fact, essential ingredients of acceleration up to PeV energies (e.g., Eq. (7) in Cristofari 2021) and are not necessarily easily combined. Expansion in a wind-blown bubble is a natural scenario to produce such a combination (Thoudam et al. 2016), and the fact that both of these SNRs appear to follow it suggests that it might not be uncommon for efficient hadronic acceleration. In this scenario, one can expect the duration of the acceleration period to be relatively short, as the shock is expected to quickly lose most of its energy upon reaching the dense bubble walls. Indeed, we note that the observed circular shape of HESS J1731−347, coinciding with dense material around the western rim (Doroshenko et al. 2017), implies that the interaction with material outside the bubble only started recently. This, and the need to have a bubble in the first place, might explain the low observed number of SNRs where hadronic acceleration to $\gg$TeV energies is plausible. Finally, we note that our findings also agree with the conclusion that GCR acceleration occurs in environments enriched by stellar outflows, explaining the observed overabundance of 22Ne/20Ne (Gupta et al. 2020).

Finally, as discussed above, the measurement of the expansion rate allows us to robustly constrain the age of the remnant, resolving the tension between earlier estimates of the age of around 30 kyr (Tian et al. 2008) and constraints on the cooling of the neutron star inside the SNR (Klochkov et al. 2015; Ofengeim et al. 2015). Our results thus strongly support the suggestion by Potekhin et al. (2020) that a much lower age of 2–6 kyr is more plausible in the context of the observed properties of the central neutron star (and, in fact, consistent with several revised estimates of the SNR age H. E. S. S. Collaboration 2011; Cui et al. 2016; Doroshenko et al. 2016). We note in passing that the revised temperature and luminosity of the CCO (Doroshenko et al. 2022) had already further reduced this tension.

Acknowledgements. The scientific results reported in this article are based to a significant degree on observations made by the *Chandra* X-ray Observatory and made use of software provided by the *Chandra* X-ray Center (CXC).

References

Acero, F., Katsuda, S., Ballet, J., & Petre, R. 2017, A&A, 597, A106
Blandford, R. D., & Ostriker, J. P. 1978, ApJ, 221, L29
Borkowski, K. J., Reynolds, S. P., Williams, B. J., & Petre, R. 2018, ApJ, 868, L21
Buchner, J. 2021, J. Open Source Softw., 6, 3001
Cao, Z., Aharonian, F. A., An, Q., et al. 2021, Nature, 594, 33
Cao, Z., Aharonian, F., An, Q., et al. 2023, ArXiv e-prints [arXiv:2305.17030]
Corso, N., Diesing, R., & Caprioli, D. 2023, ApJ, 954, 1
Cristofari, P. 2021, Universe, 7, 324
Cui, Y., Pühlhofer, G., & Santangelo, A. 2016, A&A, 591, A68
Cui, Y., Yang, R., He, X., Tam, P. H. T., & Pühlhofer, G. 2019, ApJ, 887, 47
Doroshenko, V., Pühlhofer, G., Kavanagh, P., et al. 2016, MNRAS, 458, 2565
Doroshenko, V., Pühlhofer, G., Bamba, A., et al. 2017, A&A, 608, A23
Doroshenko, V., Suleimanov, V., Pühlhofer, G., & Santangelo, A. 2022, Nat. Astron., 6, 1444
Drury, L. O., Aharonian, F. A., & Voelk, H. J. 1994, A&A, 287, 959
Fukuda, T., Yoshiike, S., Sano, H., et al. 2014, ApJ, 788, 94
Fukui, Y., Sano, H., Yamane, Y., et al. 2021, ApJ, 915, 84
Gabici, S., & Aharonian, F. A. 2014, MNRAS, 445, L70
Gupta, S., Nath, B. B., Sharma, P., & Eichler, D. 2020, MNRAS, 493, 3159
H. E. S. S. Collaboration (Abramowski, A., et al.) 2011, A&A, 531, A81
H. E. S. S. Collaboration (Abdalla, H., et al.) 2018, A&A, 612, A6
Hillas, A. M. 2005, J. Phys. G Nucl. Phys., 31, R95
Klochkov, D., Suleimanov, V., Pühlhofer, G., et al. 2015, A&A, 573, A53

Krishnamoorthy, K., & Thomson, J. 2004, J. Stat. Plan. Inf., 119, 23
Landstorfer, A., Doroshenko, V., & Pühlhofer, G. 2022, A&A, 659, A82
Ofengeim, D. D., Kaminker, A. D., Klochkov, D., Suleimanov, V., & Yakovlev, D. G. 2015, MNRAS, 454, 2668
Okuno, T., Tanaka, T., Uchida, H., et al. 2020, ApJ, 894, 50
Picquenot, A., Acero, F., Holland-Ashford, T., Lopez, L. A., & Bobin, J. 2021, A&A, 646, A82
Plucinsky, P. P., Bogdan, A., & Marshall, H. L. 2020, SPIE Conf. Ser., 11444, 1144497
Potekhin, A. Y., Zyuzin, D. A., Yakovlev, D. G., Beznogov, M. V., & Shibanov, Y. A. 2020, MNRAS, 496, 5052
Ptuskin, V., Zirakashvili, V., & Seo, E.-S. 2010, ApJ, 718, 31
Seabold, S., & Perktold, J. 2010, in 9th Python in Science Conference
Tanaka, T., Uchida, H., Sano, H., & Tsuru, T. G. 2020, ApJ, 900, L5
Taylor, J. H. 1992, Phil. Trans. R. Soc. London Ser. A, 341, 117
Thoudam, S., Rachen, J. P., van Vliet, A., et al. 2016, A&A, 595, A33
Tian, W. W., Leahy, D. A., Haverkorn, M., & Jiang, B. 2008, ApJ, 679, L85
Tsuji, N., & Uchiyama, Y. 2016, PASJ, 68, 108
Uchiyama, Y., & Aharonian, F. A. 2008, ApJ, 677, L105
Uchiyama, Y., Aharonian, F. A., Tanaka, T., Takahashi, T., & Maeda, Y. 2007, Nature, 449, 576
Weisskopf, M. C., Brinkman, B., Canizares, C., et al. 2002, PASP, 114, 1